ISSN: 2579-5821 (Print)
ISSN: 2579-5546 (Online)
URL address: http://journal.unhas.ac.id/index.php/geocelebes
DOI: 10.70561/geocelebes.v9i2.47278

Jurnal Geocelebes Vol. 9 No. 2, October 2025, 213 – 225

Shear-Wave Velocity Structure in Southeast Asia from the 2025 Mw 8.8 Kamchatka Earthquake Using Hilbert–Huang Transform

Andri Kurniawan*, Ilham Dani, Sandri Erfani

Department of Geophysical Engineering, Universitas Lampung, Bandar Lampung 35145, Indonesia.

*Corresponding author. Email: andrikurniawan@eng.unila.ac.id

Manuscript received: 20 September 2025; Received in revised form: 6 October 2025; Accepted: 17 October 2025

Abstract

The 2025 Mw 8.8 Kamchatka earthquake generated long-period teleseismic surface waves recorded at stations in Australia (CTAO), Thailand (CHTO), and Indonesia (KAPI) at epicentral distances of ~6,400–8,200 km. These records provide a useful dataset to probe crust and upper-mantle structure across contrasting Southeast Asian tectonic domains. We apply the Hilbert–Huang Transform (HHT) to vertical seismograms to extract dispersion from non-stationary wave trains. Seismograms are decomposed by empirical mode decomposition, and dispersion ridges in the Hilbert spectrum are tracked to identify frequency-dependent group arrivals. Group-velocity curves are smoothed with a low-order polynomial, and dual-frequency anchors are used to enforce phase-velocity continuity. Group velocities increase from ~3.0 km/s at periods ≥150 s to ~5.5 km/s at 40–60 s, while phase velocities span 3.3–4.6 km/s. Phase-velocity curves initialized with CRUST1.0 are inverted for 1-D shear-wave velocity (Vs), indicating crustal thicknesses of ~30–40 km: thicker beneath CHTO, intermediate at CTAO, and thinner with a slower upper mantle beneath KAPI. These lithospheric variations are consistent with regional deformation inferred from GPS and InSAR. Overall, HHT yields stable dispersion measurements and reliable Vs models relative to global references, underscoring its utility in complex tectonic regions.

Keywords: crustal thickness; dispersion analysis; Hilbert–Huang Transform; Rayleigh waves; shear-wave velocity; Southeast Asia.

Citation: Kurniawan, A., Dani, I., & Erfani, S. (2025). Shear-Wave Velocity Structure in Southeast Asia from the 2025 Mw 8.8 Kamchatka Earthquake Using Hilbert–Huang Transform. *Jurnal Geocelebes*, 9(2): 213–225, doi: 10.70561/geocelebes.v9i2.47278

Introduction

The Magnitude Moment (Mw) 8.8 Kamchatka earthquake on 29 July 2025, a major tectonic event in the Pacific Ring of Fire, generated long-period teleseismic surface waves recorded at CTAO, CHTO, and KAPI (USGS, 2025; Patton, 2025). This event generated unique teleseismic surface waves that were detected at numerous seismic stations in Southeast Asia and Australia, such as CHTO (Thailand), KAPI (Indonesia), and CTAO (Australia) (Figure 1). Long-period surface waves predominantly characterized the recordings, with epicentral distances ranging from about 6,400 to 8,200 km. This information is particularly relevant for examining the structure of the crust and upper mantle via surface-wave dispersion analysis (Li et al., 2022; Giampiccolo et al., 2024).

Surface-wave dispersion analysis has historically served as a fundamental method in seismology for extracting shear-wave velocity (Vs) beneath the Earth's surface. Due to their dispersive characteristics, phase and group velocities vary with period, allowing for the investigation of different depth ranges by meticulous analysis of dispersion curves (Babikoff & Dalton, 2019; Magrini et al., 2023; Nishida et al., 2024; Moulik &

Ekström, 2025). Traditional methodologies, including Frequency–Time Analysis (FTAN) and Short-Time Fourier Transform (STFT), have been extensively utilized in global and regional tomography research (Yang et al., 2023; Dou et al., 2024).

However, intrinsic limits constrain Fourier-based methodologies. The Fourier transform presupposes linear and stationary signals, whereas teleseismic seismograms are non-stationary, exhibiting time-varying amplitudes and frequencies. Window-based techniques like STFT offer only a constant time-frequency resolution, which may obscure significant aspects of spectrum evolution (Eriksen & Rehman, 2023). These constraints frequently diminish the precision of group-velocity measurements at extended periods, which are essential for elucidating upper-mantle structures. Therefore, more flexible options are necessary.

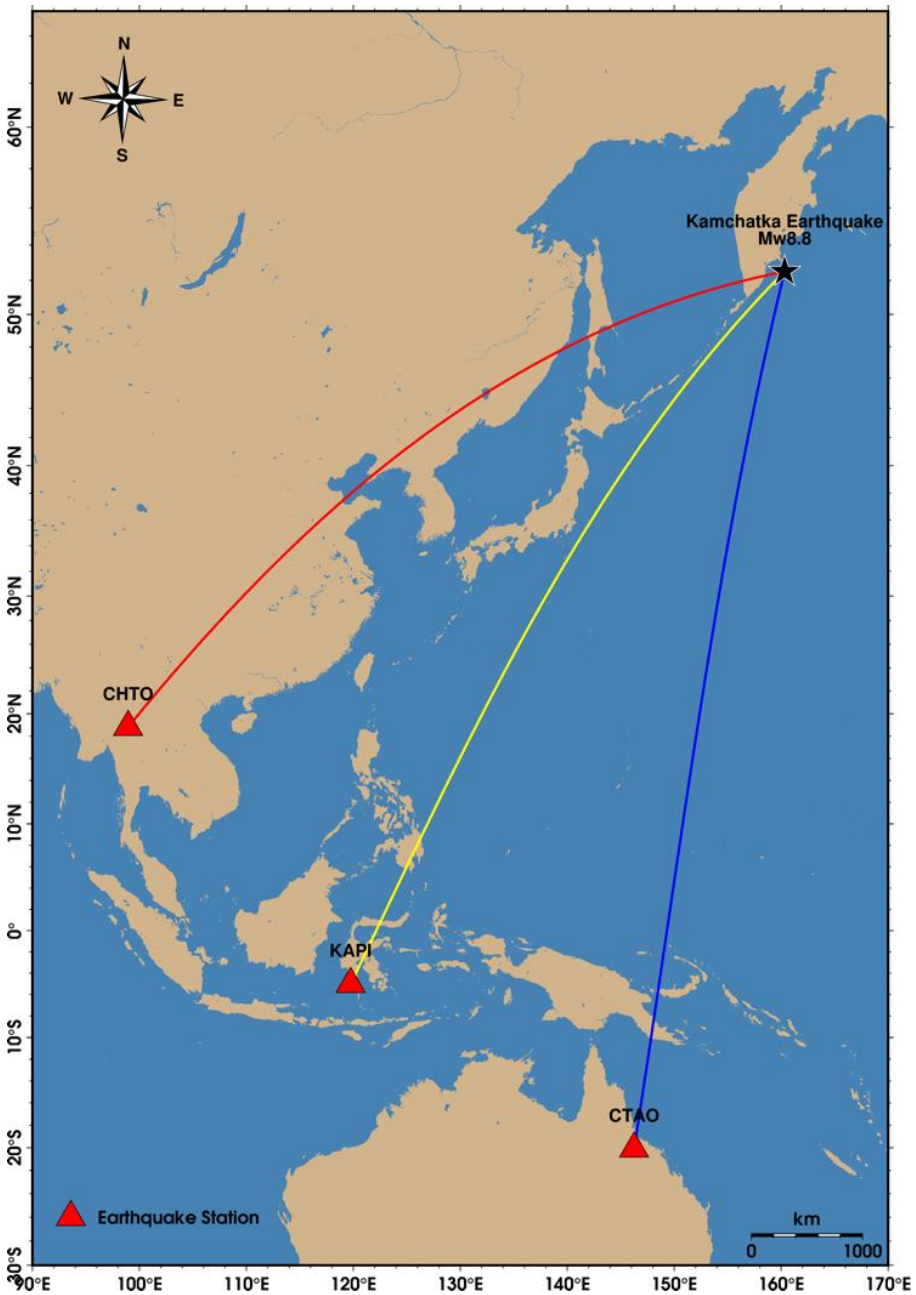

Figure 1. Map of the Mw 8.8 Kamchatka earthquake (29 July 2025) and the three GSN broadband stations analyzed: CTAO (Australia), CHTO (Thailand), and KAPI (Indonesia). Colored great-circle paths represent surface-wave propagation trajectories.

The HHT is an adaptive spectral technique that integrates Empirical Mode Decomposition (EMD) with Hilbert transform analysis to derive instantaneous frequency and amplitude from intrinsic signal components (Huang & Wu, 2008; de Souza et al., 2022; Eriksen & Rehman, 2023). Its primary advantage resides in its capacity to manage nonlinear and non-stationary data without dependence on predetermined basis functions (Harsuko et a., 2020). Chen et al. (2002) established that HHT is proficient at quantifying surface-wave group velocities and generating phase curves with considerable precision. Recent investigations, including Çakir & Kutlu (2023), emphasized that HHT can provide dependable dispersion curves even for intricate signals, hence serving as a complementing instrument to traditional FTAN-based methods.

Despite its potential, Southeast Asia still faces constraints in its implementation of HHT. Most research in Indonesia has focused on tomography utilizing ambient noise or global earthquake catalogs, whereas the systematic application of HHT to significant teleseismic events remains unaddressed. The CRUST1.0 global reference model (Laske et al., 2012) has traditionally functioned as a one-dimensional benchmark for crustal structure; yet regional evaluations and revisions of this model utilizing long-distance teleseismic data are limited in Indonesia. Due to the geological intricacies of the region, especially at the Indo-Australian and Eurasian plate boundary, discrepancies between CRUST1.0 and local conditions may be significant.

Fourier, or FTAN, methods are used in most studies of regional surface waves. These methods work best when the data is stationary, but they often have trouble with nonstationary teleseismic wave trains and single-event studies. Coverage in Southeast Asia is also spotty, and worldwide references like CRUST1.0 only give a rough idea of the structure.

We fill in these gaps by using the Hilbert–Huang Transform on vertical seismograms from the Mw 8.8 Kamchatka earthquake that happened on July 29, 2025, and was recorded at CTAO, CHTO, and KAPI. We use ridge tracking in the Hilbert spectrum to determine dispersion and the Chen et al. (2002) anchoring scheme to determine phase velocity, and we invert the curves for path-averaged 1-D Vs, starting with CRUST1.0 as a neutral global prior and using broad bounds and a stochastic global search to limit starting-model bias. We also include a simple FTAN baseline and compare it to global models. Our goal is to see if HHT gives us more steady dispersion and regionally accurate Vs than traditional Fourier-based methods.

Materials and Methods

Data

This investigation uses seismic recordings of the significant Kamchatka earthquake (Mw 8.8; July 29, 2025; 52.7°N, 160.2°E) from three broadband stations of the Global Seismographic Network (GSN): CTAO (Australia), CHTO (Thailand), and KAPI (Indonesia). The investigation centers on the vertical component (BHZ), given that fundamental-mode Rayleigh waves predominate in this channel, whereas horizontal channels are more significantly affected by Love waves and converted phases. Figure 1 illustrates the source location and ray paths, while Table 1 summarizes the station information. Waveforms and station metadata were retrieved from EarthScope Data Services (IRIS DMC) using Python (ObsPy) via FDSN web services (dataselect and station), using miniSEED and StationXML formats.

We selected CHTO, KAPI, and CTAO to sample three contrasting tectonic corridors while keeping comparable teleseismic distances and ensuring high-quality long-

period records. The criteria were clear fundamental-mode Rayleigh wave trains within the teleseismic window, adequate instrument and data quality, azimuthal diversity with respect to the source, and tectonic distinctiveness of the corridors (Büyük et al., 2020). For context, source-to-station azimuths are approximately 259° (CHTO), 225° (KAPI), and 194° (CTAO), and station elevations are ~420 m, ~300 m, and ~367 m, respectively. Paths and metadata are summarized in Figure 1 and Table 1.

Table 1. Seismic stations used in this study, including network codes, station names, geographic coordinates (°), and epicentral distances (km) from the 29 July 2025 Mw 8.8 Kamchatka earthquake.

Network Station	Latitude (°)	Longitude (°)	Epicentral Distance (km)
CTAO	-20.0883	146.255	8205
CHTO	18.8141	98.944	6430
KAPI	-5.0142	119.751	7456

Geology Regional

The seismic routes that were studied go via three different geodynamic domains: (i) the Southeast Asian margin (CHTO); (ii) the Sumatra–Sulawesi arc (KAPI), which is along the Indo-Australian subduction system; and (iii) the Australian continental margin (CTAO), which is a stable crustal lithosphere. This comparative evaluation of surface-wave velocities is made possible by the geological contrast, which emphasizes the heterogeneity of the crust and lithosphere along a transcontinental corridor. In this configuration, CHTO samples the Southeast Asian continental margin, KAPI traverses the Sunda arc and back-arc governed by Indo-Australian subduction, and CTAO lies on the stable Australian craton (Figure 1 and Table 1).

Regionally, the CHTO path crosses the Sunda land continental margin, a collage of continental blocks and volcanic arcs assembled since the Mesozoic; basin development and strike-slip belts reflect long-lived intraplate deformation within this continental core of SE Asia (Müller et al., 2019). In contrast, the KAPI path samples the Sunda arc/ back-arc, where the Indo-Australian plate subducts obliquely beneath the Sunda plate at ~50–80 mm/yr, and traverses the Sulawesi collage, where microcontinent collisions and back-arc extension produce highly heterogeneous crust and mantle structure (Hutchings & Mooney, 2021). The CTAO path lies on the Proterozoic basement of northeastern Australia (North Australian Craton) and represents stable cratonic lithosphere; regional reference models (AuSREM) indicate a comparatively smooth crust–upper-mantle structure typical of this margin.

Preprocessing

Waveforms were downloaded from the IRIS DMC at a sampling rate of 40 Hz and a recording length that exceeded 3 hours. Preprocessing procedures comprised the deconvolution of the instrument response, the removal of the mean and linear trend, and the application of a 1% taper to acquire ground displacement. To preserve Rayleigh energy from mid- to long-period, a band-pass filter was implemented at a frequency of 0.001–0.10 Hz. Subsequently, the data were downsampled to 2 Hz and trimmed to 6000 s around the primary surface-wave arrival using cascaded anti-alias filters (Figure 2). These choices preserve the target band 0.001–0.10 Hz while minimizing artifacts: detrend and demean remove offsets and drift, a 1% cosine taper reduces edge effects, and downsampling to 2 Hz after zero-phase anti-alias filtering keeps the 1 Hz Nyquist well above 0.10 Hz so no dispersion-band information is lost.

To improve data quality, short transients were removed using a median-absolute-deviation gate in the pre-event window, and we estimated signal-to-noise ratios from Hilbert amplitudes outside the Rayleigh window. Frequency choices preserve mid- to long-period Rayleigh energy while suppressing microseism and very-low-

frequency drift. Anti-alias filtering was applied before downsampling to 2 Hz.

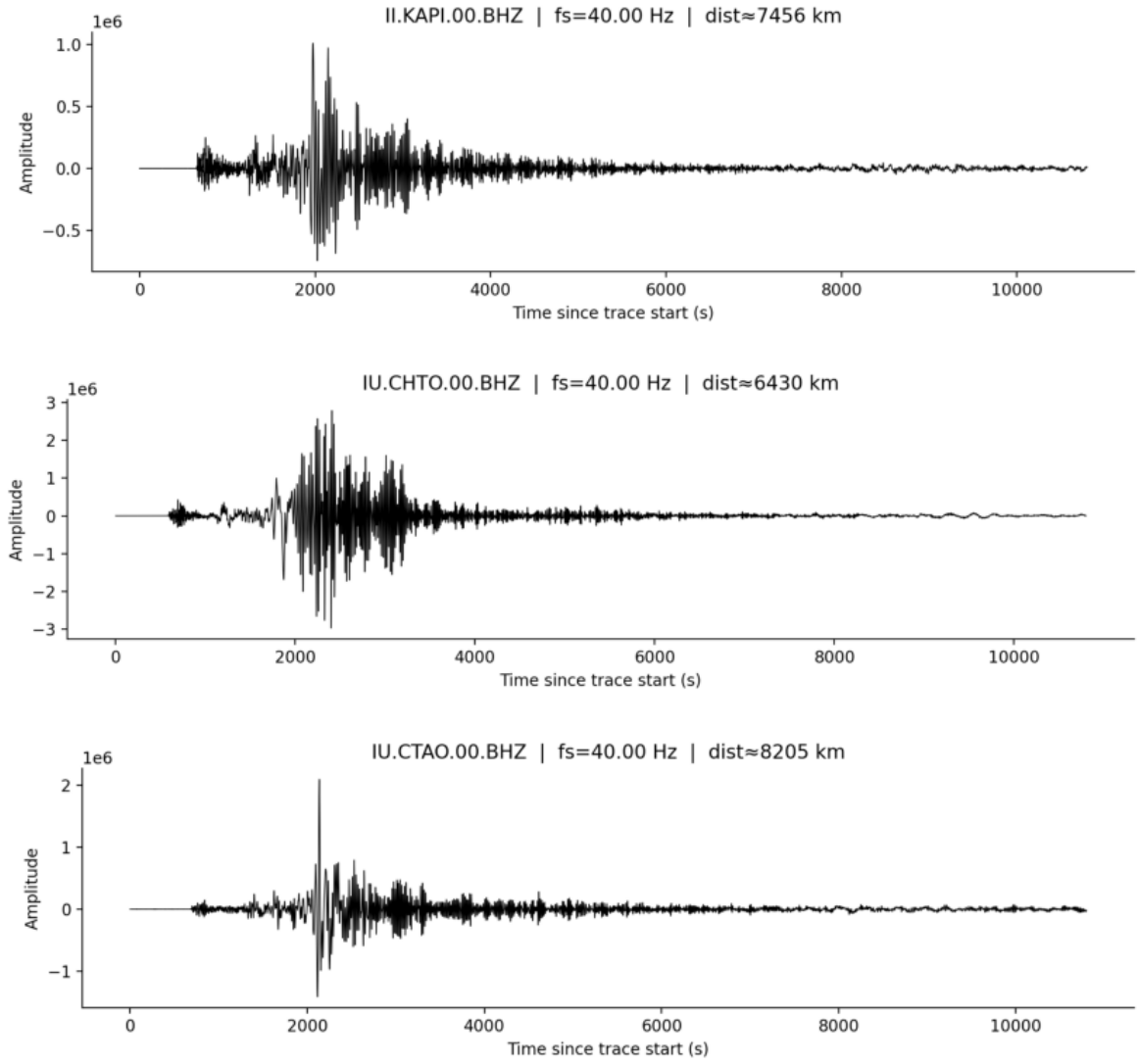

Figure 2. Vertical-component (BHZ) seismograms of the Mw 8.8 Kamchatka earthquake recorded at KAPI, CHTO, and CTAO stations after preprocessing. Distances from the epicenter range between 6,430 and 8,205 km.

Hilbert–Huang Transform

The HHT was used for adaptive spectral analysis (de Souza 2022; Eriksen & Rehman, 2023). Vertical seismograms were decomposed by EMD into intrinsic mode functions (IMFs). IMF4 typically captured sustained long-period oscillations (0.02–0.05 Hz) and was used for dispersion (Figures 3–4). We also tested adjacent modes (IMF3 and IMF5). In the 0.02–0.05 Hz band, their dispersion picks agree with IMF4 within the frequency-dependent picking uncertainty; IMF4 provides the highest SNR and the most continuous ridge, so we use it as the primary mode. Outside this band, IMF3 shows very-long-period drift and IMF5 exhibits higher-mode leakage, hence they are not used. The sifting stopped at a standard-deviation threshold of 0.2 or at ten sifts, and end effects were reduced by symmetric mirroring and spline envelopes. The analytic signal is (Huang & Wu, 2008):

$$z(t) = x(t) + i\,\hat{x}(t) \qquad (1)$$

where x(t) is the original signal and ẋ(t) is its Hilbert transform. The instantaneous frequency is (Huang & Wu, 2008):

$$f(t) = \frac{1}{2\pi}\frac{d\phi}{dt} \qquad (2)$$

The Hilbert spectrum was computed on overlapping windows to stabilize ridge continuity; windows that failed continuity or had Signal-to-Noise Ratio (SNR) > 3 were rejected. Let A(*t*,*f*) be the Hilbert amplitude. We restrict the search to a Rayleigh-wave window defined by the epicentral distance and a 2–5.5 km/s group-velocity bracket. For each frequency f, the group arrival time is (Chen et al., 2002),

$$t_{\text{peak}}(f) = \arg\max_{t \in W_R} A\,(t, f) \qquad (3)$$

The picked track is median-filtered (three bins) and spline-smoothed; samples that break window-to-window continuity or fail SNR > 3 are discarded. Choosing the amplitude maximum follows the modal ridge where Rayleigh energy concentrates and approximates the stationary-phase group delay, making it less sensitive than centroids to leakage, side lobes, or mode interference. The variance across overlapping windows is carried forward as frequency-dependent measurement weights for the inversion.

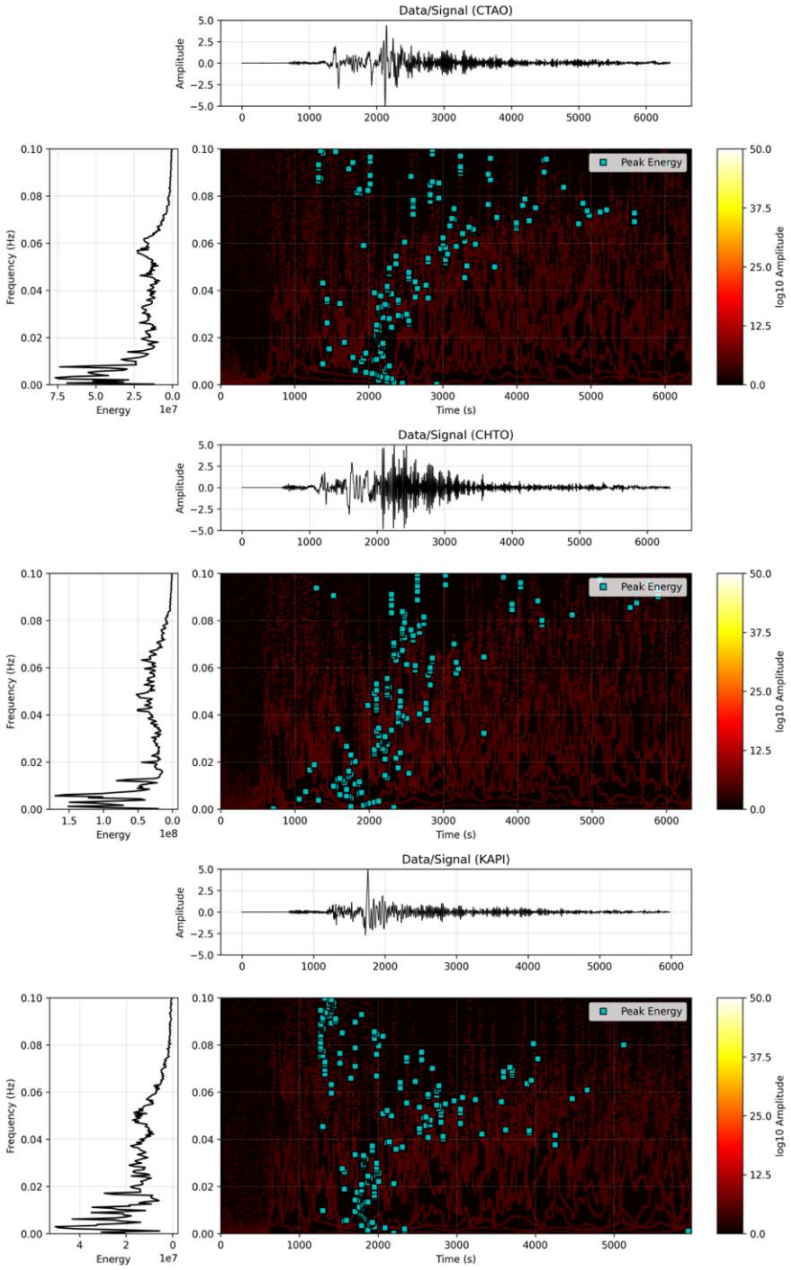

Figure 3. Hilbert spectra of vertical seismograms at CTAO, CHTO, and KAPI stations. Blue markers indicate ridge picks corresponding to the arrival of fundamental-mode Rayleigh energy.

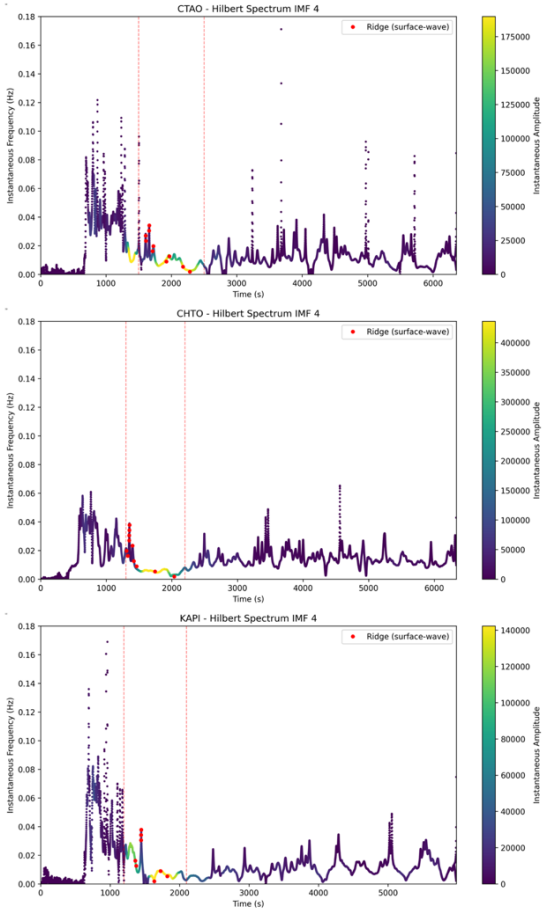

Figure 4. IMF4 Hilbert spectra at CTAO, CHTO, and KAPI stations. Red dots mark the extracted ridges used for group-delay measurements, while color shading denotes instantaneous amplitude.

Phase-Velocity Reconstruction and Vs Inversion

The group velocity was determined by the arrival timings of the ridges (Neukirch et al. 2021):

$$U(f) = \frac{X}{t_{peak}(f)} \quad (4)$$

where the epicentral distance is denoted by X (Table 1). A second-order (quadratic) polynomial is applied to $U(f)$ to suppress scatter while preserving long-period trends (Figures 5–6). Smoothing is needed to suppress high-frequency jitter from windowed picking and noise that would otherwise propagate into phase reconstruction and inversion. We choose a low-order polynomial because path-averaged dispersion varies smoothly with frequency; a low order preserves the broad trend and avoids spline-type wiggles. The order is kept minimal so residuals stay within the picking uncertainty, and features such as the Rayleigh minimum are not shifted.

The formulation of Chen et al. (2002) was followed for phase-velocity reconstruction:

$$\phi(f) = 2\pi \int_{f0}^{f} T_g(v)dv + \phi_0, \quad (5)$$

$$c(f) = \frac{\omega X}{\phi(f) - 2\pi N}, \quad \omega = 2\pi f \quad (6)$$

where N corrects for the 2π ambiguity and ϕ_0 is set by a dual-frequency anchor to ensure physical continuity. A low-order polynomial is used to remove small oscillations not resolvable by the data and to keep the group–phase pair mutually consistent (Figure 7).

For each path, the reconstructed $c(f)$ is inverted for a 1-D Vs profile. The initial model is taken from CRUST1.0 (Laske et al., 2012); forward modeling uses DISBA for the fundamental Rayleigh mode (Carchedi et al., 2025). The objective function combines a Huber misfit with smoothness and weak prior terms (Çakir & Kutlu, 2023),

$$J(m) = \sum_i \rho\delta\left(\frac{c_i^{obs} - c_i^{syn}(m)}{\sigma_i}\right) + \lambda\sum_j (V_{s,j+1} - V_{s,j})^2 + \beta\sum_{j\epsilon crust}(V_{s,j} - V_{s,j}^{(0)})^2 \quad (7)$$

where σ_i are frequency-dependent weights derived from the variance across overlapping windows, λ enforces profile smoothness, and β prevents unrealistic drift from the CRUST1.0 crust while not enforcing it. Long-period data (≳200 s) are emphasized to improve upper-mantle sensitivity; shorter periods provide secondary constraints (Figure 7).

We invert a path-averaged layered model with free Vs and layer thicknesses, including a free Moho depth; compressional velocity and density follow CRUST1.0 and are fixed. Parameter bounds are deliberately broad and guided

by period–depth sensitivity so the solution is driven by the dispersion data. The misfit uses the Huber loss with the frequency-dependent weights σ_i in Equation (7). Models are explored with a stochastic global search (Differential Evolution) with early stopping; small smoothness and prior terms stabilize the solution without enforcing CRUST1.0.

Results and Discussion

The Hilbert spectrum obtained from vertical-component decomposition indicates a distinct concentration of energy in the 20–200 s time region. Of the seven IMFs derived from EMD, IMF4 consistently demonstrated stable oscillations and the predominance of the fundamental-mode Rayleigh energy across all stations. The time-frequency maps (Figures 3–4) show continuous ridges, which were then taken out to identify arrival timings that depend on frequency. This method produces a clearer picture of dispersion than traditional Fourier-based methods that use fixed windowing (Huang et al., 1998; Huang & Wu, 2008; Khan et al., 2025) and its effectiveness is in line with recent Indonesian studies employing surface-wave dispersion techniques for Vs mapping (Putri et al., 2025).

Figures 5 and 6 show that group-velocity curves at CTAO and CHTO follow the same trend. At lengthy periods (>150 s), group velocities range from 3.0 to 3.5 km/s. At periods of 40–60 s, they rise to about 5.0–5.5 km/s. The dashed curves in Figure 5 denote second-order polynomial smoothing; trials with first- and third-order fits produced changes within the picking uncertainty. This pattern is due to the fact that fundamental-mode Rayleigh waves are more sensitive to depth than other types of waves (Babikoff & Dalton, 2019; Moulik & Ekström, 2025). Polynomial smoothing worked well to smooth out noise, especially at low frequencies.

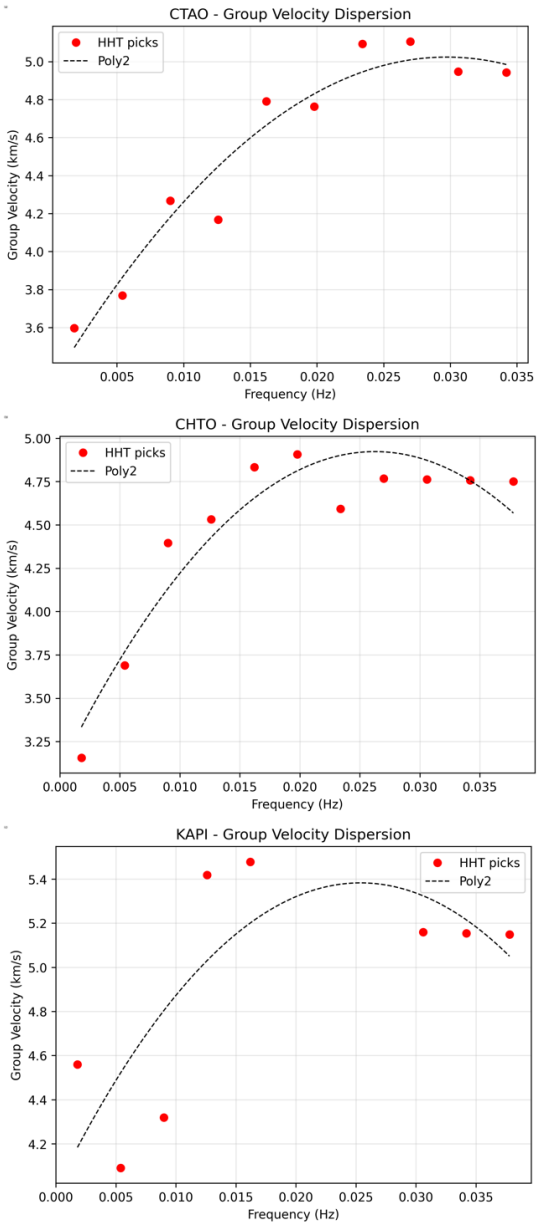

Figure 5. Group-velocity dispersion curves U(f) extracted from Hilbert–Huang ridges at CTAO, CHTO, and KAPI. Black dots represent observed ridge picks, and dashed lines show low-order polynomial smoothing.

Figure 6 shows the reconstructed phase-velocity curves using the Chen et al. (2002) formulation. They are stable in the frequency band of 0.004–0.04 Hz, with values between 3.3 and 4.6 km/s. CTAO and CHTO both show the U-shaped pattern of fundamental Rayleigh waves, with a velocity minimum between 0.005 and 0.01 Hz, which is in line with what has been seen around the world (Ritzwoller & Levshin, 1998; Yang et al., 2023). The data at KAPI, however, do not follow this trend. Instead,

they indicate an almost constant increase in speed with no clear minimum. Possible reasons for such variations include contamination from higher modes, incorrectly assigning the integer N in the Chen et al. (2002) formulation, or tectonic complexity along the Sumatra path that makes ridge extraction less stable. Such anomalies heighten inversion uncertainty and underscore the necessity for enhanced anchoring procedures and more rigorous data quality control (Xiao et al., 2022; Çakır & Kutlu, 2023).

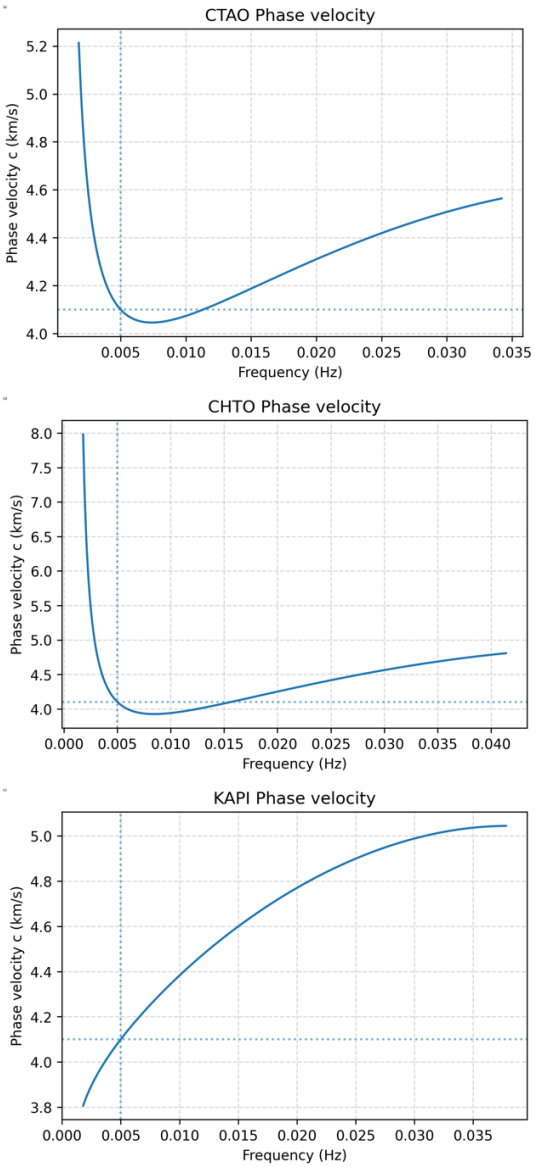

Figure 6. Phase-velocity curves c(f) reconstructed using the Chen et al. (2002) method for CTAO, CHTO, and KAPI. Gray dashed lines indicate uncertainty bounds.

The 1-D Vs inversion of the phase-velocity curves (Figure 7) indicates clear lateral differences among the three source–station paths. Here we define the crustal boundary (Moho) as the depth of the strongest positive Vs gradient that marks the transition from crustal to upper-mantle velocities in the inverted 1-D profile. The reported depth is read from the best-fitting model and is consistent with the period–depth sensitivity of the data.

At CTAO on the Australian continental margin, we infer ~35 km crust and relatively fast upper-mantle Vs (~4.6–4.7 km/s); together with smooth long-period dispersion and low inversion misfit, these observations are consistent with a cool, mechanically strong lithosphere at this margin. CHTO in mainland Southeast Asia shows a thicker crust (~40 km), in line with regional tomography (Dou et al., 2024). In contrast, KAPI in Indonesia indicates a thinner crust (~30–32 km) and a slower upper mantle, likely reflecting a weaker lithosphere associated with the ongoing Indo-Australian subduction. These patterns broadly agree with regional deformation from GPS and InSAR (Yang et al., 2023; Chen et al., 2025), while uncertainties remain larger at KAPI due to lower SNR and limited long-period constraints.

Overall, the data indicate significant variation in the lithosphere and crust across the transcontinental corridor. The tectonic difference between stable continental interiors and active subduction zones is shown by a thick crust in Southeast Asia, a rapid mantle under the Australian margin, and a weak lithosphere under Sumatra. The HHT and Chen-phase reconstruction method effectively generated stable dispersion curves from non-stationary waveforms. This technique led to Vs inversion findings that better reflect regional structure than the global CRUST1.0 reference (Laske et al., 2012). This method makes it possible to use dispersion analysis in areas with

complicated tectonics, and it lays the groundwork for future investigations in Southeast Asia on a regional scale. Similar approaches have also been successfully applied in Indonesian contexts for shallow crustal characterization using MASW (Putri et al., 2025), further underscoring the broader applicability of surface-wave dispersion methods.

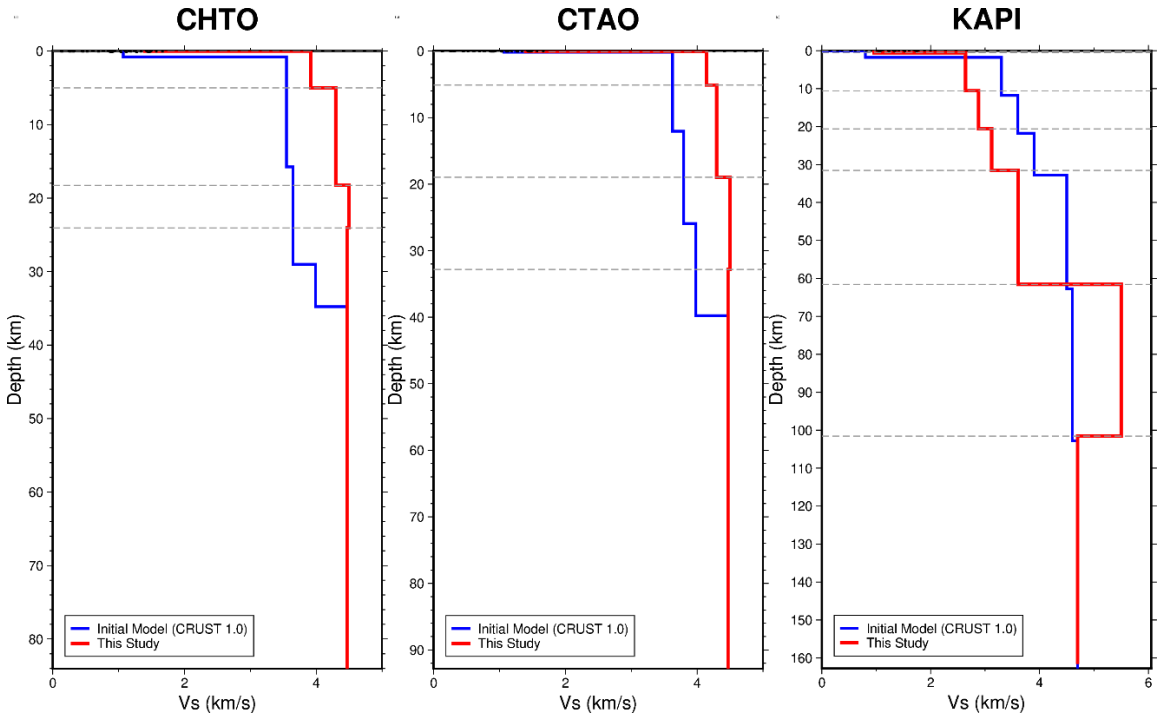

Figure 7. Inverted 1-D Vs models beneath CTAO, CHTO, and KAPI (red lines) compared with the CRUST1.0 reference model (blue lines). Moho discontinuities appear as velocity jumps at 30–40 km depth.

Conclusions

We tested the idea that an HHT workflow can extract stable dispersion from non-stationary teleseismic waves and produce Vs models that reflect regional geology. The results support this idea. Ridge tracking on the Hilbert spectrum presents continuous group and phase curves at CHTO in Thailand, KAPI in Indonesia, and CTAO in Australia. These three paths represent a continental margin, an arc and back-arc, and a craton.

We invert the dispersion using a neutral global prior and recover coherent lateral changes. The crust is thicker beneath the Southeast Asian margin, of intermediate thickness toward the Australian margin, and thinner with a slower upper mantle beneath Sulawesi. Accuracy and robustness follow from the inversion design. We use broad parameter bounds and a stochastic global search to limit dependence on the starting model. We also propagate dispersion-picking uncertainty with frequency-dependent weights and examine period–depth sensitivity to confirm that the data can resolve the reported features.

These findings are useful beyond method testing. The path-specific dispersion and Moho constraints can sharpen starting models and regularization in regional surface-wave tomography and can improve velocity structures and crustal corrections for seismic-hazard simulations in Southeast Asia. Future work will stack multiple events and add azimuthal analyses to examine anisotropy and to stabilize the longest periods.

Acknowledgements

This research did not receive any specific grant from funding agencies in the public,

commercial, or not-for-profit sectors. The authors gratefully acknowledge the IRIS Data Management Center (DMC) for providing open access to the seismic data used in this study. We also thank the journal editor and anonymous reviewers for their constructive comments, which helped improve the quality of this manuscript.

Author Contribution

Andri Kurniawan led the research, including conceptualization, methodology design, data collection and curation, software development, formal analysis, visualization, and preparation of the original draft. Ilham Dani contributed to validation and assisted with manuscript review and editing. Sandri Erfani provided supervision and contributed to manuscript review and editing.

Conflict of Interest

There were no funds or finances exchanged in this study, neither among the authors nor between the parties involved in the research. so that the author can explain it to the Journal of Geocelebes' rules.

References

Babikoff, J. C., & Dalton, C. A. (2019). Long-period Rayleigh wave phase velocity tomography using USArray. *Geochemistry, Geophysics, Geosystems*, 20(4), 1990–2006. https://doi.org/10.1029/2018GC008073

Büyük, E., Zor, E., & Karaman, A. (2020). Joint modeling of Rayleigh wave dispersion and H/V spectral ratio using Pareto-based multiobjective particle swarm optimization. *Turkish Journal of Earth Sciences*, 29, 684–695. https://doi.org/10.3906/yer-2001-15

Çakir, Ö., & Kutlu, Y. A. (2023). Forward modeling the group and phase velocities of Rayleigh and Love surface waves beneath Central Anatolia: Fifth parameter for transverse isotropy. *Malaysian Journal of Geosciences,* 7(2), 134–149. https://doi.org/10.26480/mjg.02.2023.134.149

Carchedi, C. J. W., Gaherty, J. B., Byrnes, J. S., Rondenay, S., Steckler, M. S., Ajala, R., Persaud, P., Sandvol, E. A., Alim, M. S., Singha, S., & Akhter, S. H. (2025). Evolving sediment structure and lithospheric architecture across the Indo-Burman forearc margin from the joint inversion of surface- and scattered-wave seismic constraints. *Journal of Geophysical Research: Solid Earth,* 130(6), e2024JB030050. https://doi.org/10.1029/2024JB030050

Chen, C.-H., Li, C.-P., & Teng, T.-L. (2002). Surface-wave dispersion measurements using Hilbert–Huang transform. *Terrestrial, Atmospheric and Oceanic Sciences,* 13(2), 171–184. https://doi.org/10.3319/TAO.2002.13.2.171(T)

Chen, Y., Li, J., Lu, K., & Hu, T. (2025). Coseismic slip model and early post-seismic deformation processes of the 2024 M7.5 Noto Peninsula, Japan earthquake revealed by InSAR and GPS observations. *Geophysical Journal International*, 240(2), 1048–1063. https://doi.org/10.1093/gji/ggae429

de Souza, U. B., Escola, J. P. L., & Brito, L. d. C. (2022). A survey on Hilbert–Huang transform: Evolution, challenges and solutions. *Digital Signal Processing*, 120, 103292. https://doi.org/10.1016/j.dsp.2021.103292

Dou, H., Xu, Y., Lebedev, S., Chagas de Melo, B., van der Hilst, R. D., Wang, B., & Wang, W. (2024). The upper mantle beneath Asia from seismic tomography, with inferences for the mechanisms of tectonics, seismicity, and magmatism. *Earth-Science Reviews*, 255, 104841.

https://doi.org/10.1016/j.earscirev.2024.104841

Eriksen, T., & Rehman, N. U. (2023). Data-driven nonstationary signal decomposition approaches: A comparative analysis. *Scientific Reports,* 13, 1798. https://doi.org/10.1038/s41598-023-28390-w

Giampiccolo, E., Tuvè, T., Bianco, F., & Del Pezzo, E. (2024). Depth and spatial variation of the shear-wave attenuation parameters in the shallow crust and lower crust/upper mantle of Mt. Etna (Italy). *Pure and Applied Geophysics*, 181, 171–187. https://doi.org/10.1007/s00024-023-03400-0

Harsuko, M. R. C., Zulfakriza, Z., Nugraha, A. D., Sarjan, A. F. N., Widiyantoro, S., Rosalia, S., Puspito, N. T., & Sahara, D. P. (2020). Investigation of Hilbert–Huang transform and Fourier transform for horizontal-to-vertical spectral ratio analysis: Understanding the shallow structure in Mataram City, Lombok, Indonesia. *Frontiers in Earth Science*, 8, 334. https://doi.org/10.3389/feart.2020.00334.

Huang, N. E., & Wu, Z. (2008). A review on Hilbert–Huang transform: Method and its applications to geophysical studies. *Reviews of Geophysics,* 46(2), RG2006. https://doi.org/10.1029/2007RG000228

Hutchings, S. J., & Mooney, W. D. (2021). The seismicity of Indonesia and tectonic implications. *Geochemistry, Geophysics, Geosystems*, 22(9), e2021GC009812. https://doi.org/10.1029/2021GC009812

Khan, S. B., Balajee, A., Shah, S. S. M., Mahesh, T. R., Alojail, M., & Gupta, I. (2025). A novel ensemble empirical decomposition and time–frequency analysis approach for vibroarthrographic signal processing. *Circuits, Systems, and Signal Processing*. https://doi.org/10.1007/s00034-025-03096-8

Laske, G., Masters, G., Ma, Z., & Pasyanos, M. E. (2012). CRUST1.0: An updated global model of Earth's crust. *Geophysical Research Abstracts,* 14, EGU2012-3743-1. https://meetingorganizer.copernicus.org/EGU2012/EGU2012-3743-1.pdf

Li, M., Song, X., Li, J., & Bao, X. (2022). Crust and upper mantle structure of East Asia from ambient noise and earthquake surface wave tomography. *Earthquake Science,* 35(2), 71–92. https://doi.org/10.1016/j.eqs.2022.05.004

Magrini, F., Kästle, E., Pilia, S., Rawlinson, N., & De Siena, L. (2023). A new shear-velocity model of continental Australia based on multi-scale surface-wave tomography. *Journal of Geophysical Research: Solid Earth,* 128(7), e2023JB026688. https://doi.org/10.1029/2023JB026688

Müller, R. D., Zahirovic, S., Williams, S. E., Cannon, J., Seton, M., Bower, D. J., Tetley, M. G., Heine, C., Le Breton, E., Liu, S., Russell, S. H. J., Yang, T., Leonard, J., & Gurnis, M. (2019). A global plate model including lithospheric deformation along major rifts and orogens since the Triassic. *Tectonics*, 38, 1841–2157. https://doi.org/10.1029%2F2018TC005462

Moulik, P., & Ekström, G. (2025). Radial structure of the Earth: (II) Model features and interpretations. *Physics of the Earth and Planetary Interiors*, 361, 107320. https://doi.org/10.1016/j.pepi.2025.107320

Neukirch, M., García-Jerez, A., Villaseñor, A., Luzón, F., Ruiz, M., & Molina, L. (2021). Horizontal-to-vertical spectral ratio of ambient vibration obtained by

Hilbert–Huang transform. *Sensors,* 21(9), 3292. https://doi.org/10.3390/s21093292

Nishida, K., Takagi, R., & Takeo, A. (2024). Ambient noise multimode surface wave tomography. *Progress in Earth and Planetary Science,* 11, 4. https://doi.org/10.1186/s40645-023-00605-8

Patton, J. R. (2025). *Earthquake report: M 8.8 Kamchatka*. EarthJay. https://earthjay.com/?p=12355

Putri, A. C. P., Refrizon, R., Hadi, A. I., & Al Ansory, A. R. (2025). Mapping of soil stability based on Vs30 using MASW on Kalimantan Highway, Bengkulu City. *Jurnal Geocelebes,* 9(1), 1–14. https://doi.org/10.70561/geocelebes.v9i1.34956

U.S. Geological Survey. (2025). *M 8.8—Kamchatka Peninsula, Russia earthquake*. USGS Earthquake Catalog. https://earthquake.usgs.gov/earthquakes/eventpage/us6000qw60

Xiao, X., Sun, L., Wang, X., & Wen, L. (2022). Simultaneous inversion for surface-wave phase velocity and earthquake centroid parameters: Methodology and application. *Journal of Geophysical Research: Solid Earth,* 127(9), e2022JB024018. https://doi.org/10.1029/2022JB024018

Yang, X., Luo, Y., Jiang, C., Yang, Y., Niu, F., & Li, G. (2023). Crustal and upper mantle velocity structure of SE Tibet from joint inversion of Rayleigh wave phase velocity and teleseismic body wave data. *Journal of Geophysical Research: Solid Earth,* 128(7), e2022JB026162. https://doi.org/10.1029/2022JB026162